VIRTUAL ANGIOGRAPHY USING CFD SIMULATIONS BASED ON PATIENT-SPECIFIC PARAMETER OPTIMIZATION

Juergen Endres[1], *Thomas Redel*[2], *Markus Kowarschik*[2], *Jana Hutter*[1,3], *Joachim Hornegger*[1,3], *Arnd Doerfler*[4]

[1]Pattern Recognition Lab, University of Erlangen-Nuremberg, Erlangen, Germany
[2]Siemens AG, Healthcare Sector, Forchheim, Germany
[3]Erlangen Graduate School in Advanced Optical Technologies (SAOT), Erlangen, Germany
[4]Department of Neuroradiology, University of Erlangen-Nuremberg, Erlangen, Germany

ABSTRACT

Computational fluid dynamics (CFD) simulations of blood flow within intracranial aneurysms may provide important hemodynamic information for treatment planning. However, reliable validation is required prior to applications in clinical environments. For that purpose, we introduce a workflow for generating virtual digital subtraction angiographies (DSA) based on CFD results and real patient-individual contrast injection protocols. This allows for comparing virtual and acquired DSA and thus drawing first conclusions about the reliability of the CFD simulation. Due to the possibility of simulating arbitrary x-ray system angulations, both mechanically impossible angulations as well as multiple projection views are representable using the proposed virtual DSA workflow.

Index Terms— CFD, hemodynamics, virtual angiography

1. INTRODUCTION

In recent years, planning of intracranial aneurysm treatment has increasingly been based on patient-specific data. In addition to anatomical information, hemodynamics plays a major role. Since physical quantities such as wall shear stress, velocities, etc. can currently not be measured *in vivo*, efforts have been put into computational fluid dynamics (CFD) simulations to obtain such information. However, validating CFD simulations in patients remains a severe problem due to the lack of ground truth data.

A first step to verify the plausibility of the CFD result is by creating a simulated or virtual angiography, as was first proposed by Ford et al. in 2005 [1], and comparing the virtual angiography to an acquired one representing real patient blood flow. To obtain insight into the influence of several patient-specific parameters, further studies focused on simulating *in vitro* blood flow of phantoms [2] as well as patient data [3, 4].

In this paper, a workflow for creating multiple view virtual angiographies based on discrete particle methods is introduced, methods of comparing 2D DSA series are discussed, and first results of our work are presented. From real angiography, contrast injection information will be extracted and then used to define the boundary conditions for virtual angiography.

2. MATERIALS AND METHODS

An overview of the workflow is shown in figure 1. As input data, a 3D rotational angiography (3DRA) provides geometric information, whereas a 2D DSA series acquired at 30 fps (Artis zee biplane, Siemens AG) is used to extract information for defining boundary conditions such as heart rate and contrast bolus injection profile, used for both the CFD simulation and the virtual angiography (section 2.4). The virtual angiography itself is performed under the assumption of a passive transport model based on advection and diffusion. Both steps (sections 2.2 and 2.3) are performed using discrete particle tracing methods.

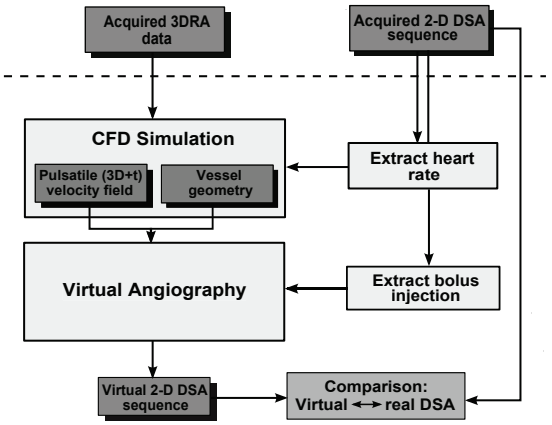


Fig. 1. Virtual angiography workflow.

2.1. CFD simulation

For performing pulsatile CFD simulation, preprocessing steps include surface mesh generation based on the 3DRA data and selection of the inlet and outlet boundaries. While a pulsatile inflow profile was adapted based on [5], zero pressure outlet conditions were selected.

Within the CFD solver, the rigid geometry is transformed into a level-set representation for solving the Navier-Stokes equations, as described in [6]. Under the assumption of a Newtonian behavior of blood, viscosity was chosen to be 0.004 Pa s with a density of 0.00105 $\mathrm{g/mm^3}$ [5, 6]. The resulting 4D velocity field was then used as an input for subsequent virtual angiography computations.

2.2. Advection of contrast agent

In our implementation, contrast agent is modelled as a set of mass- and dimensionless particles $\Omega = \{\boldsymbol{\rho}_i\}, i \in \{1, ..., n\}$, where $\boldsymbol{\rho}_i \in \mathbb{R}^3$ denotes a single particle freely movable in space (not restricted

to grid points), and $n \in \mathbb{N}$ is the total number of used particles. Velocities at certain locations $\boldsymbol{v}(\boldsymbol{x}), \boldsymbol{x} \in \mathbb{R}^3$ are calculated using linear interpolation applied on the CFD velocity grid. All particles Ω are advected using a fixed time step δt, meeting the Courant-Friedrichs-Lewy condition [7] for stability reasons.

The trajectory of a single particle $\boldsymbol{\rho}_i(t)$ is specified by a first order ordinary differential equation $\dot{\boldsymbol{\rho}}_i(t) = f(t, \boldsymbol{\rho}_i(t))$ and solved using an explicit fourth order Runge-Kutta scheme [8]. Initial conditions are satisfied by placing particles $\boldsymbol{\rho}_i$ at time points $T_{\boldsymbol{\rho}_i,0}$ within the predefined cross-sectional inlet area.

To obey the law of conservation of mass, particles whose trajectory is crossing the vessel wall are bounced back into the vessel, whereas particles leaving the vessel through an outlet are discarded.

2.3. Diffusion of contrast agent

According to Fick's law of diffusion, diffusive flux of contrast agent is proportional to the concentration gradient in the regarded medium:

$$\boldsymbol{J} = -D\frac{\partial C}{\partial \boldsymbol{x}}, \tag{1}$$

where $\boldsymbol{J}$ denotes the diffusive flux, D the diffusivity constant, and C the contrast agent concentration, which is created by continuizing the discrete particle set Ω:

$$C(\boldsymbol{x}) = \sum_{i=1}^{n} g(\boldsymbol{\rho}_i), \qquad \boldsymbol{\rho}_i \in \Omega. \tag{2}$$

Here, $g(\boldsymbol{x})$ denotes a density distribution, for which a Gaussian distribution is chosen.

C is then sampled on a regular grid for numerically computing a gradient vector field, which is needed for modelling the diffusive flow of contrast agent. This movement of particles is performed using the algorithm described in section 2.2, for which the currently calculated vector field $\boldsymbol{J}$ is used as the underlying velocity field.

2.4. Extraction of heart rate and bolus injection

For this purpose, a time-intensity curve integrated for a certain user-defined line of interest (LOI) is created in the real DSA at the location of the selected inflow boundary of the CFD mesh (see figure 2, top and center). First, based on this data, a temporal distance Δt between successive intensity peaks is estimated and used for calculating the heart rate.

Second, the time-intensity curve is used for deriving the bolus injection curve to be used as input for the virtual angiography. In order to get rid of the underlying pulsatile pattern, which is not related to the injection process itself, the inflow of contrast agent is assumed to behave like a capacitor function [3]. This function is then iteratively fitted to the measured data using the Levenberg-Marquardt optimization algorithm.

2.5. Arbitrary view projection geometry

For comparing and evaluating real and virtual angiographies, the projection view for reprojecting the concentration volume onto an image plane is generated such that both the virtual and the real angiographies display the angiograms from the same camera position. Generally, arbitrary projection geometries are possible, which allow to generate multiple DSA series, even from angulations which are mechanically impossible in reality. As shown in figure 3, this may lead to additional information about hemodynamics and facilitate further (real) DSA acquisitions by exhibiting C-arm angulations for which interesting anatomical spots are clearly visible.

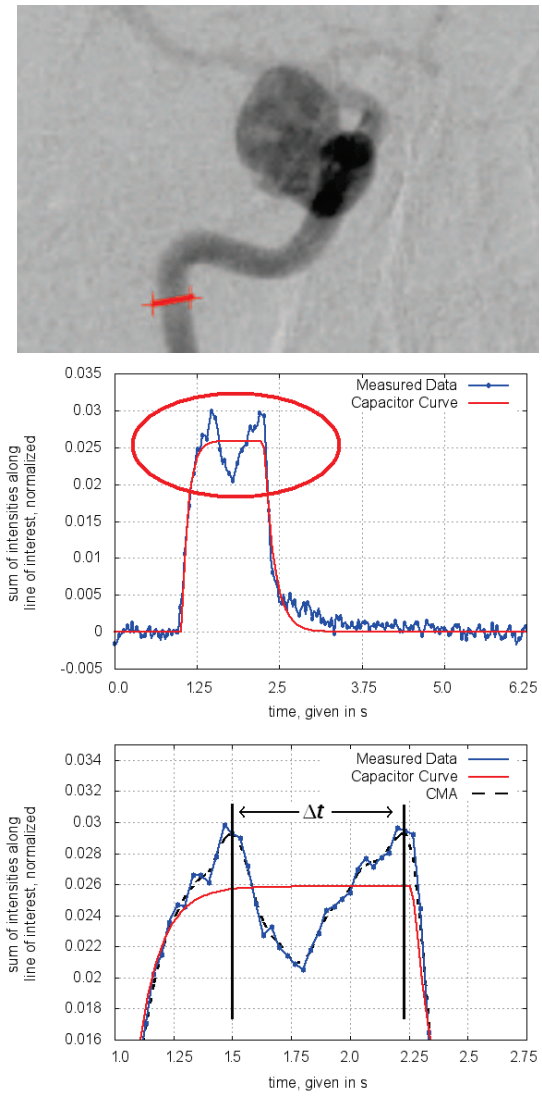
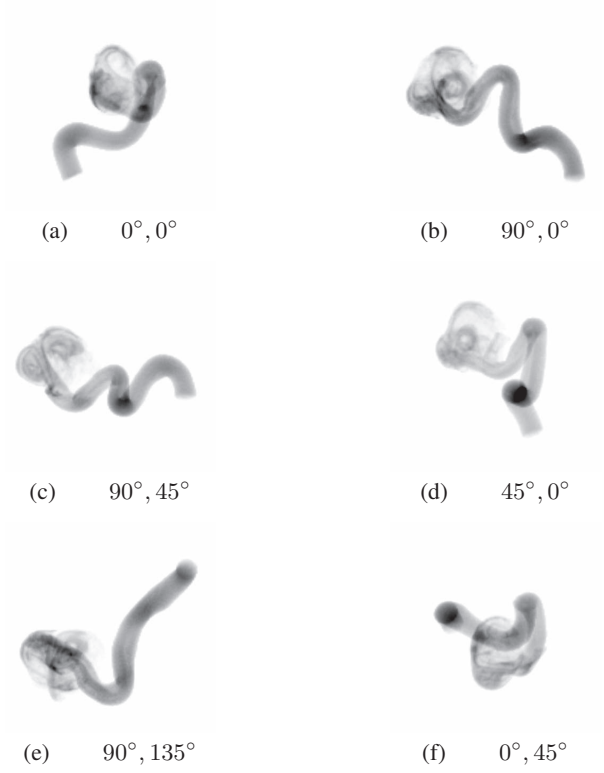


Fig. 2. Large paraophthalmic aneurysm of the right internal carotid artery (DSA). Top: LOI defining the inlet area. Center: time-intensity curve of a 2D DSA series and fitted capacitor curve model. Bottom: zoomed view of center image, schematic representation of heart rate extraction; in this image, the black curve represents the central moving average (CMA).

3. RESULTS

The workflow was evaluated on two patient data sets showing real intracranial aneurysms at the internal carotid artery. In addition to the 3DRA data, two 2D DSA series with varying C-arm angulations were used for each case. The 2D DSA series show the complete in- and outflow of contrast agent acquired at a constant frame rate of 30fps.

Based on the results of the patient-specific CFD simulations, virtual angiographies were generated using a total number of 10^6 par-



(a) $0°, 0°$ (b) $90°, 0°$

(c) $90°, 45°$ (d) $45°, 0°$

(e) $90°, 135°$ (f) $0°, 45°$

Fig. 3. Different projection angles of one simulated angiography. All images show the current contrast agent distribution at time $t = 2.1s$. The simulated position of the C-arm is denoted below each image, given as $\{$*primary angle, secondary angle*$\}$, where *primary angle* denotes a rotation around the anteroposterior axis and *secondary angle* around the left-right axis.

ticles per virtual angiography. Results were compared on a qualitative (depicted in figure 4 for patient A) as well as on a quantitative basis: for this purpose, we restrict ourselves to the comparison of time-intensity curves (TICs) in predefined regions of interest (ROIs) (figure 5). These time-intensity curves were normalized such that intensities range from 0 to 100. The measured quantities are the full widths at half maximum (FWHM) of the real and virtual angiographies (table 1).

In figure 4, the virtual and real angiography is shown for patient case A. The angiographies are well-synchronized concerning the time and the structure of contrast agent flow: The inflow jet is clearly visible, it enters at $t = 1.4s$ the aneurysm at the bottom side and circulates counterclockwise at the aneurysm wall. At $t = 2.5s$, the inflow of contrast agent stops in both angiographies. As can be seen at $t = 3.8s$, the contrast agent flushes out quite fast in the virtual angiography, whereas in the real angiography, the contrast agent has an extended residence time — this is presumably caused due to certain mixing effects [9] which are not covered by our model yet.

The measured time-intensity curves support this observation, see figure 5: the rising and trailing edges for real and virtual angiographies are in good correspondence for ROI1 and ROI2. For ROI3, the outflow phase is extended for the real angiography. Taking a closer look at the pulsatility of the time-intensity curves, both the real and the virtual angiography have similar durations between succeeding

patient A

DSA sequence	ROI	FWHM real DSA	FWHM virtual DSA
DSA1	ROI1	1.27s	1.30s
	ROI2	1.23s	1.30s
	ROI3	2.87s	1.70s
DSA2	ROI1	1.25s	1.29s
	ROI2	1.39s	1.32s
	ROI3	2.21s	1.68s

patient B

DSA sequence	ROI	FWHM real DSA	FWHM virtual DSA
DSA1	ROI1	0.56s	0.60s
	ROI2	0.60s	0.63s
	ROI3	0.69s	0.66s
DSA2	ROI1	0.53s	0.59s
	ROI2	0.56s	0.63s
	ROI3	0.63s	0.69s

Table 1. Quantitative measurements: full widths at half maximum (FWHM) of real and virtual DSA. The regions of interest (ROI1-ROI3) are depicted for patient case A in figure 5.

intensity peaks; however, these peaks are not coinciding perfectly since no synchronization of the start of the injection and the actual heart phase at beginning of the simulation is performed.

Concerning the FWHM, the presented results also show a good agreement between real and simulated angiographies; again, values from ROI3 differ for patient case A in terms of an extended outflow phase: compared to the acquired data, the virtual FWHM is for the first DSA sequence decreased by $1.17s$ or 41%. For other ROIs, a maximum of $0.07s$, corresponding to the duration of approximately 2 image frames, are measured.

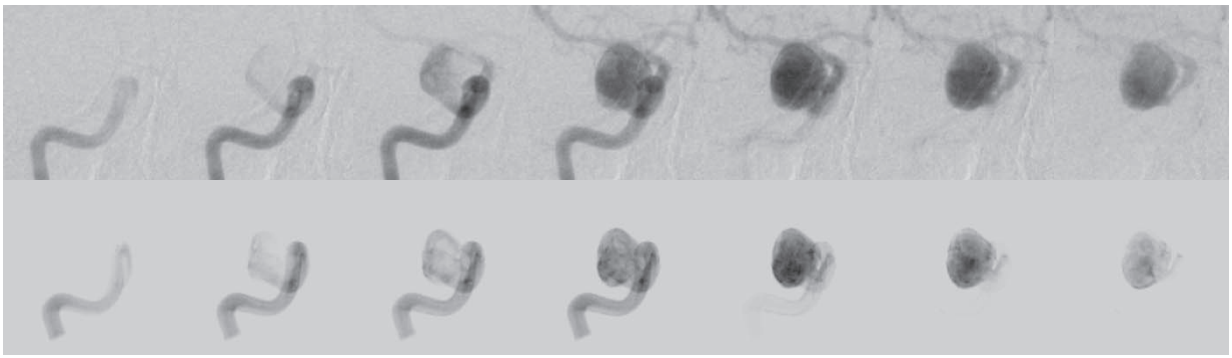
4. DISCUSSION & CONCLUSION

We presented a workflow for creating virtual angiographies based on CFD simulation results to evaluate the plausibility of the CFD simulation. To allow for comparison with available real patient DSA, contrast characteristics at the inflow boundary were extracted and used as boundary conditions within the framework.

Additionally, the proposed workflow allows for the generation of virtual angiographies with arbitrary angulations. As this relies on computation only, no additional contrast agent or x-ray dose are needed.

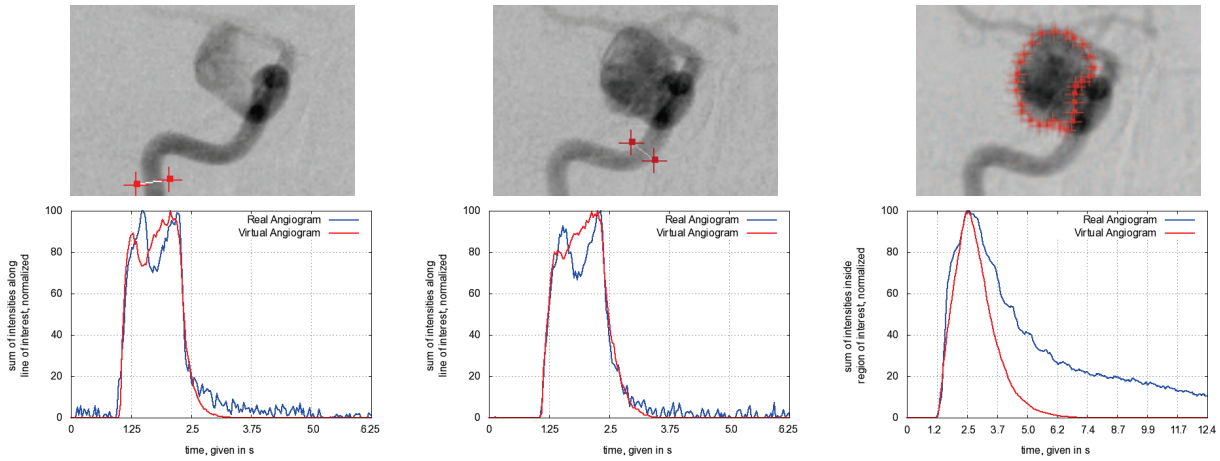
The presented preliminary results show a promising correspondence and provide the possibility for future work investigating the validation of CFD simulation results. Additional parameter optimization concerning the visual appearance, e.g. the contrast intensities in both scenarios, may improve the similarity between both angiographies.

We observed certain effects in real angiographies that are currently not reproducable in virtual angiographies using the proposed workflow. Future work will investigate these effects and focus on an advancement of the CFD simulation by improving further patient-specific boundary conditions, with the use of simulated angiographies.



(a) $t = 1.2s$ (b) $t = 1.4s$ (c) $t = 1.5s$ (d) $t = 1.9s$ (e) $t = 2.7s$ (f) $t = 3.1s$ (g) $t = 3.8s$

Fig. 4. A real (top) and a virtual (bottom) angiography. The current state is denoted below the images.



(a) ROI1 (b) ROI2 (c) ROI3

Fig. 5. Time-intensity curves of virtual (red) and real (blue) angiographies at the inlet boundary (ROI1), at short distance behind the inlet (ROI2), and at a ROI defined by the aneurysm (ROI3). The time-intensity curves were normalized such that intensities range from 0 to 100.

5. REFERENCES

[1] M.D. Ford, G.R. Stuhne, H.N. Nikolov, D.F. Habets, S.P. Lownie, D.W. Holdsworth, and D.A. Steinman, "Virtual angiography for visualization and validation of computational models of aneurysm hemodynamics," *IEEE Trans. Med. Imag.*, vol. 24, no. 12, pp. 1586–1592, 2005.

[2] Qi Sun, Alexandra Groth, Matthias Bertram, Irina Waechter, Tom Bruijns, Roel Hermans, and Til Aach, "Phantom-based experimental validation of computational fluid dynamics simulations on cerebral aneurysms," *Medical Physics*, vol. 37, no. 9, pp. 5054–5065, 2010.

[3] Qi Sun, A. Groth, I. Waechter, O. Brina, J. Weese, and T. Aach, "Quantitative evaluation of virtual angiography for interventional x-ray acquisitions," in *IEEE International Symposium on Biomedical Imaging*, 2009, pp. 895 –898.

[4] J. R. Cebral, A. Radaelli, A. Frangi, and C. M. Putman, "Qualitative comparison of intra-aneurysmal flow structures determined from conventional and virtual angiograms," in *Society of Photo-Optical Instrumentation Engineers (SPIE) Conference Series*, march 2007, vol. 6511 of *Presented at the Society of Photo-Optical Instrumentation Engineers (SPIE) Conference*.

[5] M. Spiegel, T. Redel, Y.J. Zhang, T. Struffert, J. Hornegger, R.G. Grossman, A. Doerfler, and C. Karmonik, "Tetrahedral vs. polyhedral mesh size evaluation on flow velocity and wall shear stress for cerebral hemodynamic simulation," *Computer Methods in Biomechanics and Biomedical Engineering*, vol. 14, no. 1, pp. 9–22, 2011.

[6] V. Mihalef, R. I. Ionasec, P. Sharma, B. Georgescu, I. Voigt, M. Suehling, and D. Comaniciu, "Patient-specific modelling of whole heart anatomy, dynamics and haemodynamics from four-dimensional cardiac ct images," *Interface Focus*, 2011.

[7] R. Courant, K. Friedrichs, and H. Lewy, "On the partial difference equations of mathematical physics," *IBM Journal of Research and Development*, vol. 11, pp. 215–234, 1967.

[8] J.C. Butcher, *Numerical Methods for Ordinary Differential Equations*, John Wiley and Sons, Ltd, 2005.

[9] L.-D. Jou, A. Mohamed, D.H. Lee, and M.E. Mawad, "3d rotational digital subtraction angiography may underestimate intracranial aneurysms: Findings from two basilar aneurysms," *American Journal of Neuroradiology*, vol. 28, pp. 1690–1692, 2007.